PET/MRI of atherosclerosis

Review Article on Advanced Imaging in The Diagnosis of Cardiovascular Diseases

PET/MRI of atherosclerosis

Mueez Aizaz[1,2], Rik P. M. Moonen[1,2], Jochem A. J. van der Pol[1], Claudia Prieto[3,4], René M. Botnar[3,4], M. Eline Kooi[1,2]

[1]Department of Radiology and Nuclear Medicine, Maastricht University Medical Center, Maastricht, The Netherlands; [2]CARIM School for Cardiovascular Diseases, Maastricht University, Maastricht, The Netherlands; [3]School of Biomedical Engineering and Imaging Sciences, King's College London, London, UK; [4]Escuela de Ingenieria, Pontificia Universidad Catolica de Chile, Santiago, Chile

Contributions: (I) Conception and design: M Aizaz, RPM Moonen, ME Kooi; (II) Administrative support: None; (III) Provision of study materials or patients: None; (IV) Collection and assembly of data: None; (V) Data analysis and interpretation: None; (VI) Manuscript writing: All authors; (VII) Final approval of manuscript: All authors.

Correspondence to: Prof. Dr. M. Eline Kooi. Department of Radiology and Nuclear Medicine, Maastricht University Medical Center, Universiteitssingel 50, level 1, room 1.328, P. O. Box 5800, 6202 AZ Maastricht, The Netherlands. Email: eline.kooi@mumc.nl.

Abstract: Myocardial infarction and stroke are the most prevalent global causes of death. Each year 15 million people worldwide die due to myocardial infarction or stroke. Rupture of a vulnerable atherosclerotic plaque is the main underlying cause of stroke and myocardial infarction. Key features of a vulnerable plaque are inflammation, a large lipid-rich necrotic core (LRNC) with a thin or ruptured overlying fibrous cap, and intraplaque hemorrhage (IPH). Noninvasive imaging of these features could have a role in risk stratification of myocardial infarction and stroke and can potentially be utilized for treatment guidance and monitoring. The recent development of hybrid PET/MRI combining the superior soft tissue contrast of MRI with the opportunity to visualize specific plaque features using various radioactive tracers, paves the way for comprehensive plaque imaging. In this review, the use of hybrid PET/MRI for atherosclerotic plaque imaging in carotid and coronary arteries is discussed. The pros and cons of different hybrid PET/MRI systems are reviewed. The challenges in the development of PET/MRI and potential solutions are described. An overview of PET and MRI acquisition techniques for imaging of atherosclerosis including motion correction is provided, followed by a summary of vessel wall imaging PET/MRI studies in patients with carotid and coronary artery disease. Finally, the future of imaging of atherosclerosis with PET/MRI is discussed.

Keywords: Atherosclerosis; hybrid imaging; PET/MRI; vascular; vulnerable plaque

Submitted Dec 09, 2019. Accepted for publication Feb 05, 2020.
doi: 10.21037/cdt.2020.02.09
View this article at: http://dx.doi.org/10.21037/cdt.2020.02.09

Introduction

Atherosclerosis is characterized by the formation of plaques in arterial walls (1). These atherosclerotic plaques can cause narrowing of the arterial lumen, reducing the amount of oxygen-rich blood reaching the organs, and in case of severe luminal stenosis, cause perfusion defects. More importantly, these plaques can rupture and cause thrombus formation and embolization, which can result in myocardial infarction or stroke (1).

Cardiovascular diseases (CVDs) are the number one cause of death globally. Of the 18 million people who died from CVDs in 2016, 85% died from a heart attack or stroke (2). Apart from the mortality and morbidity, CVDs are also a huge economic burden. The global costs for CVDs are estimated to rise from US $863 billion in 2010 to US $1,044 billion in 2030 (3).

Numerous factors such as increased levels of low-density lipoproteins (LDL), elevated blood pressure, higher levels of hemostatic factors, family history of CVD, gender (4) unhealthy diet, lack of exercise and smoking (5) have been recognized as risk factors for the development of

atherosclerosis.

Atherosclerotic plaques most often develop in regions with arterial damage, curvatures or bifurcations with disturbed blood flow. The wall shear stress exerted by blood flow in these regions is decreased. Endothelial cells exposed to lower wall shear stress are nonuniformly shaped, resulting in poor cell to cell contact (6,7), making these sites more susceptible to LDL extravasation across the endothelial layer. The deposited lipoproteins undergo oxidative modification in the intimal layer, inducing an inflammatory response (8). Monocytes from the lumen and smooth muscle cells (SMCs) also migrate to the intimal layer. The oxidized LDL accumulates in monocytes-derived macrophages, transforming them into foam cells. Foam cells undergo apoptosis and form a lipid-rich necrotic core (LRNC). SMCs in this pro-inflammatory and hyperlipidemic environment produce extracellular matrix which forms the fibrous tissue of the plaque including the fibrous cap overlying the LRNC. Metabolic activity from macrophages in the intimal layer creates an increased oxygen demand. This state of hypoxia triggers angiogenesis (9). New microvessels grow from the adventitia into the plaque to supply oxygen and other nutrients to the developing lesion (9,10). These microvessels have poor structural integrity and blood-derived inflammatory cells can easily leak through the endothelial cell layer further contributing to plaque inflammation. The immature microvessels have also been suggested to contribute to intraplaque hemorrhage (IPH) (11), although it was recently shown that plaques with IPH show less leaky plaque microvessels (12). Micro-calcifications arising from extracellular vesicles from macrophages and SMCs (13,14) can also be found in the developing atherosclerotic plaque.

A plaque prone to rupture is referred to as a vulnerable plaque. A vulnerable plaque is characterized by the presence of a large LRNC, inflammation, microvasculature, IPH, and a thin or ruptured fibrous cap (15). Plaque rupture is the underlying cause in approximately 60% of sudden coronary deaths (16) and approximately 20% of ischemic strokes (17). For patients with carotid artery disease, the onset of cerebrovascular symptoms and degree of stenosis are the main deciding factors to select the appropriate treatment. A stenosis of <50% is categorized as mild, 50% to 69% as moderate and 70% to 99% as severe according to NASCET criteria (18). Based on clinical trials performed in the 1990's, for symptomatic patients with 50% or higher stenosis, the number of patients needed to undergo carotid revascularization to prevent one ipsilateral stroke in 5 years is 9 for men versus 36 for women (19). Studies have shown that apart from degree of stenosis, other vulnerable plaque components can be used as independent predictors of cerebrovascular events (20-23). A recent meta-analysis by Schindler *et al.* showed that the presence of IPH in carotid plaques is an independent risk predictor for ipsilateral ischemic stroke in both symptomatic and asymptomatic patients that is stronger than any known clinical risk factor (20).

Non-invasive imaging provides tremendous opportunities to identify vulnerable plaques (24-26). Magnetic resonance imaging (MRI), with its superior soft tissue contrast is ideal to identify vulnerable plaque components, although this is still challenging for coronary plaques. A meta-analysis by Gupta *et al.* (23) found that IPH, LRNC and thin or ruptured fibrous cap as determined by MRI, demonstrated a hazard ratio of 4.59 [95% confidence interval (CI), 2.91–7.24], 3.00 (95% CI, 1.51–5.95), and 5.93 (95% CI, 2.65–13.20) respectively, for future stroke or transient ischemic attack. Positron emission tomography (PET) with radiolabeled tracers can visualize the molecular changes that occur in a plaque. Marnane *et al.* (27) and Kelly *et al.* (21) showed that ^{18}F-FDG uptake on PET can independently predict recurrent stroke. The development of hybrid PET/MRI have opened new avenues for early diagnosis, improved risk stratification and treatment evaluation of patients with atherosclerosis.

The aim of this paper is to review the current status and future potential of hybrid PET/MRI of atherosclerotic plaques. The advantages and disadvantages of different types of hybrid PET/MRI systems are summarized. Technical developments which can further improve cardiovascular PET/MRI are discussed. An overview of clinical PET/MRI studies in patients with coronary and carotid artery disease is given. Finally, we discuss the future potential of PET/MRI for imaging atherosclerosis.

PET, MR and PET/MRI

MRI

MRI is based on magnetic properties of protons. When a patient is shifted into the scanner, a small net magnetization will arise in the patient in the direction of the external magnetic field of the MRI system. This net magnetization can be manipulated using radiofrequency (RF) pulses in combination with magnetic field gradients. After changing the net magnetization with an RF coil, relaxation of the net magnetization back to equilibrium will occur and the

change in transversal magnetization is measured with an RF coil. These relaxation processes, i.e., T1 (longitudinal direction) and T2 relaxation (transversal direction), can be used to generate T1 weighted (T_1w) or T2 weighted (T_2w) images. Numerous MRI pulse sequences have been developed to optimize the signal, contrast or to shorten the scan time (28).

PET imaging

In PET imaging, patients are injected with a radiolabeled tracer, which emits positrons. A positron subsequently annihilates with an electron producing two photons moving in the opposite direction, which are detected by the PET detectors, creating an image of the tracer concentration inside the patient. As the annihilation photons pass through different tissues on their way to the PET detector, they get attenuated. Photon attenuation can cause severe artifacts in PET images and therefore, needs to be corrected. Attenuation correction is performed using attenuation maps. These maps represent the attenuation coefficients (μ) of different tissues. Standalone PET detectors use a transmission source with known activity to create an attenuation map (29).

Commonly, PET images are quantified by calculating the standard uptake value (SUV) which is the ratio of activity concentration of a region of interest (ROI) to the whole-body activity concentration. Target to background ratio (TBR), which is the SUV in the tissue of interest normalized to blood-pool activity, is also used for quantification of PET images (30). Based on the temporal resolution of PET detectors, PET scanners can have time-of-flight (TOF) capability, which allows the use of the time interval between the detection of the two annihilation photons to improve the estimation of where on the line of response the annihilation occurred. This improves the signal to noise ratio (SNR) and spatial resolution of the PET images (31,32).

Sequential *vs.* simultaneous PET/MRI

Technical details about the development of PET/MRI systems have been previously reviewed (33). A major challenge in the development of hybrid PET/MRI systems was the functioning of the photomultiplier tubes (PMTs) in the strong magnetic field from the MRI (34). The first solution to this problem was the sequential PET/MRI approach with a bed that moves between the PET and MRI system. The distance between the two gantries and extra shielding around the PET components, ensures that the PET detectors are not affected by the strong magnetic field (35). Both systems can be present in the same room or in different rooms (36). This solution is relatively economical since no drastic changes in the design of the scanners is required. Also, PET performance is similar to PET in PET/CT scanners (37). In the two-room approach, attenuation maps are created using CT, whereas in the other approach, attenuation maps are created using MRI. Co-registration of PET and MR images is better than separate PET and MRI scans, but any motion from the patient between the scans can make image fusion difficult. Similarly, involuntary motion such as breathing or cardiac motion can cause misregistration between the two scans. Another disadvantage of this approach is that relatively larger rooms are required to host the scanner (38).

The second approach is an integrated PET/MR scanner, which allows simultaneous PET and MRI scans. The PMTs were replaced by avalanche photodiodes (APD) (39) or silicon photomultipliers (SiPMs) (40), which are not affected by magnetic fields. This approach suffers from even less misregistration errors. MRI-based motion information can be used for PET motion correction as well. Simultaneous scans also mean reduced scan time and thus more comfort for the patient. The SiPM based PET detectors have superior time resolution (0.4 ns) (34) enabling TOF PET capability (41).

Attenuation correction for PET in PET/MRI

MR based attenuation correction in PET/MRI has been comprehensively reviewed by Mehranian *et al.* (42). Attenuation maps for the reconstruction of PET images were another challenge towards PET/MRI being widely accepted for clinical use. As contrast in CT images is based on differences in photon attenuation, CT images can be used to create attenuation maps (43). Contrarily, MR images are based on proton density and relaxation times of different tissues, and so cannot be directly used for creating attenuation maps. Additionally, in MRI scans it is challenging to differentiate between bone (high attenuation) and air (low attenuation). The field of view (FOV) of the MRI scanner in the transverse plane is typically smaller than the PET FOV, which can cause truncation artifacts. This truncation occurs in the off-center regions, such as the arms besides the body. Arms are a source of attenuation and need to be considered in the generation of attenuation maps. A common approach to generate attenuation maps

based on MR images is using an MRI Dixon sequence to create water and fat-based images, which are then pixelwise segmented into air, lung, fat and soft tissue. Linear attenuation coefficients are assigned to each tissue class (44). To visualize bones (short T_2 times) ultrashort echo time (UTE) (45) and zero echo time (ZTE) (46) sequences can be used. One approach to counter truncated MR-based attenuation correction maps, is to use B0 homogenization using gradient enhancement (HUGE) (47). This technique utilizes an optimum readout gradient to compensate for B0 inhomogeneities and gradient non-linearities. Using this technique, an increase of up to 60 cm in FOV, and a change of up to 30% in SUV was reported (48). Template-based attenuation correction technique utilizes an MR image as template and a co-registered PET attenuation template generated from transmission scans. Using non-linear registrations, the MR template is first registered to the MR image of the patient and then the same registrations are used to transform the PET attenuation template into an attenuation map (36). The atlas-based approach uses an atlas with MR and matching CT images. The CT images are used to generate an attenuation atlas at 511 keV. The MR images from the atlas are registered to the MR images of the patient under observation and the same transformation is applied to the CT based attenuation atlas. These transformed pseudo-CT images can be used as an attenuation map for the patient to reconstruct PET images. Any anatomical anomalies in the patient and their effects on attenuation are not taken into account with this method (49). Another approach exploits the fact that PET data contains both attenuation and activity information, and thus creates an attenuation map based on only PET data using a maximum likelihood attenuation and activity (MLAA) algorithm (50). One of the many uses of artificial intelligence (AI) based techniques in the imaging domain is image transformation, for instance transformation of MR images into pseudo CT images (51,52). Considering the creation of pseudo CT attenuation maps or MLAA μ-maps from MR images as an image transformation problem, deep learning presents a viable solution to create attenuation maps from different input sources (MR images, MLAA μ-maps, non-attenuation corrected PET images) (53-58).

RF-coils are invisible on MR images but are a source of PET photon attenuation (59,60). The attenuation by the RF-coils needs to be considered when creating attenuation corrected PET images. For rigid coils such as the head and neck coil, CT or transmission-based attenuation maps can be used. However, surface coils such as the dedicated carotid coils are usually flexible and don't have a fixed position, thus using a standard attenuation map is not straightforward. One solution is to use markers to locate the position and shape of the coil in MR images and subsequently use non-rigid transformations to transform a CT based attenuation map of the coil (61). Another solution is to use dedicated PET/MRI coils which reduce photon attenuation for the ROI by making design changes and less attenuating materials (62,63).

Numerous oncology studies have compared the diagnostic performance of PET/MRI with PET/CT. Consensus among these studies is that despite the differences in attenuation correction methods, statistically significant strong positive correlations between SUV measurements from PET/MR and PET/CT exist (64-66). It is important to note here that a significant underestimation (67) and overestimation (68) of SUV values on the PET/MRI have been reported. A limitation of these studies is that the order in which the PET/CT and PET/MRI examination were performed was not randomized. The SUV values are also affected by pharmacokinetics, i.e., biological uptake and clearance, differences between scanner technologies, data processing algorithms, type of attenuation correction used, PET acquisition times and the time between tracer injection and the second scan (67,69,70).

Cardiovascular motion correction or compensation

MRI

For a detailed review on cardiac and respiratory motion and the techniques used to minimize or correct for motion, we refer to the following reviews (71-75). Vessel wall imaging requires sub-millimeter spatial resolution. Consequently, slight motion during image acquisition can already cause motion artifacts. Motion correction is especially important for coronary imaging. Apart from their small size, these vessels are constantly in motion because of breathing and cardiac motion. Carotid vessel wall MRI can also suffer from motion artifacts due to the pulsating motion of the arteries, effects of swallowing and patient motion.

The scan time to perform high spatial resolution coronary artery imaging is too long to be performed within a single breath-hold for patients with coronary artery disease, which is why free breathing techniques are preferred (73). Free breathing acquisitions can be

acquired by measuring the respiratory signal with an external device (respiratory bellows) and performing prospective or retrospective respiratory gating (76). Another approach is the use of 1-dimensional (1D) MR navigators, positioned on the liver-diaphragm interface to perform respiratory gating and tracking (77). This 1D navigator measures the position of the liver-diaphragm interface, based on which the window with the least respiratory motion is selected. A major limitation of the 1D diaphragmatic navigator in combination with respiratory gating is that it leads to long and unpredictable scan times, due to low scan efficiency. Several self-navigation and image-navigator based techniques have been proposed to achieve 100% scan efficiency (no gating, no data rejection). 1D self-navigation techniques extract respiratory motion information often from the repeatedly acquired k-space center line. The Fourier transform of this signal, referred to as superior inferior (SI) projection, is used for translational respiratory motion tracking. Each projection acquired is then compared to a chosen reference projection to estimate and to retrospectively correct for the SI position of the heart over time (78). Self-navigated signals estimate the motion from projection data that include static tissues and thus may affect the accuracy of the motion signal. 2D and 3D image navigators (79-81) separate static and moving tissues and enable motion estimation/correction in multiple dimensions. These approaches can be self-gated (employing the startup echoes of the main acquisition) or based on acquiring low spatial resolution images every heartbeat before cardiac MR acquisition and have been used to correct for 2D/3D translational motion prospectively and retrospectively. These approaches can be combined with bin-to-bin non-rigid motion correction (incorporated directly in the reconstruction) (82-84) or respiratory-resolved reconstruction (85,86) to account for the complex motion of the heart. Cardiac motion is commonly tackled using electro-cardiogram (ECG)-based gating. The ECG signal is used to identify the region of the cardiac cycle with the least motion, which is where the acquisition window is placed. This duration is generally not long enough to acquire the entire k-space in one go; therefore, the acquisition is done in a segmented fashion over multiple cardiac cycles. Alternatively, with free running techniques, acquisition is not performed in any particular phase of the cardiac cycle but throughout. The ECG signal is recorded simultaneously, to retrospectively sort the k-space readouts into different bins for reconstruction (87). An alternative approach is to estimate cardiac phases from the self-gating signal directly as has been shown in several studies (88,89).

PET

Detailed information on different sources of motion and how to minimize, characterize and compensate them for both PET and MRI can be found in reviews by Catana *et al.* (72) and by Munoz *et al.* (74). Like MRI, respiratory and cardiac motion are the two main sources of motion in cardiovascular PET imaging. Deriving the respiratory signal from an external device or from PET counts (90) allows binning of the PET data. Similarly, using the ECG signal, the cardiac cycle can also be divided into multiple phases. Individual bin data can be reconstructed, and then transformed using rigid or non-rigid transformations to a reference position, before being averaged into one static image. This approach is called the reconstruct-transform-average approach (74,91). Another approach is the motion-compensated image reconstruction, where the transformations are incorporated in the PET system model, resulting in motion-corrected PET images after reconstruction (92,93).

PET/MRI

Simultaneous PET/MRI provides a unique opportunity to apply MRI-based motion correction on both MRI and PET images. Munoz *et al.* (94) utilized a non-rigid respiratory motion-compensated CMRA approach (based on 2D iNAV for respiratory binning) to correct for respiratory motion induced cardiac motion in the simultaneously acquired PET and MR data. For the MR images, on average the visible length of the right coronary artery and left anterior descending artery increased by 45.53% and 75.45%, and sharpness by 56.44% and 51.11% respectively, when applying the proposed technique compared to no motion correction (*Figure 1*). For PET images the proposed technique outperformed no motion correction in terms of noise and mean SUV and outperformed a gated approach in terms of noise (*Figure 2*).

Robson *et al.* used MR images to create cardiac and respiratory motion models, to correct for respiratory and cardiac motion in PET images (90). The motion-corrected PET images were compared with non-motion-corrected-non-gated and dual gated (respiratory and cardiac gated) PET images. The TBR and contrast to noise ratio (CNR) were significantly larger for motion-corrected PET (2.8±0.9, 21±22) compared to non-motion-corrected-non-gated PET (2.4±0.9, P=0.0001; 15±13, P=0.02), while TBR was lower and CNR greater

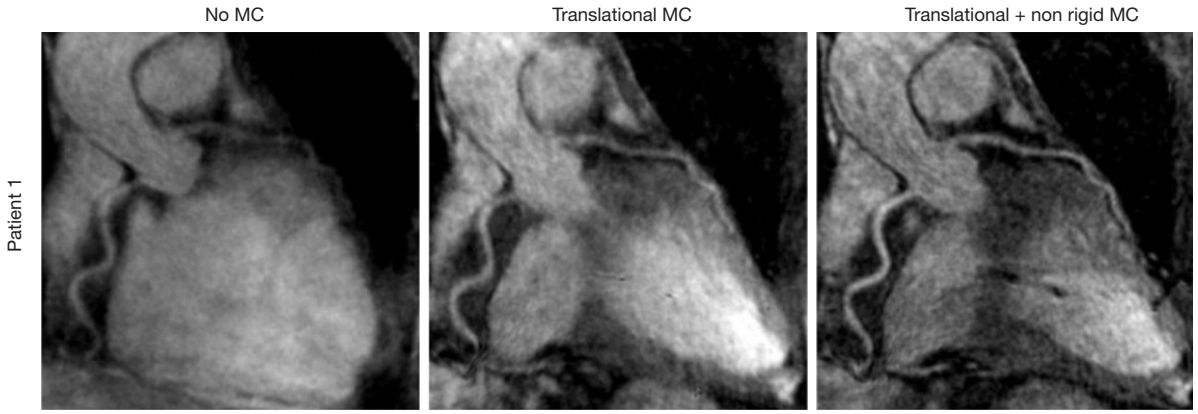

Figure 1 Coronary images from an oncology patient showing the left anterior descending artery and right coronary artery with motion correction (MC), only translational motion correction, and translational motion correction and non-rigid motion correction. Improvements in the visualization of the vessels are observed when applying translational MC, and further improvements are observed with translation and non-rigid MC. [Images reproduced with permission from Munoz *et al.* (94)].

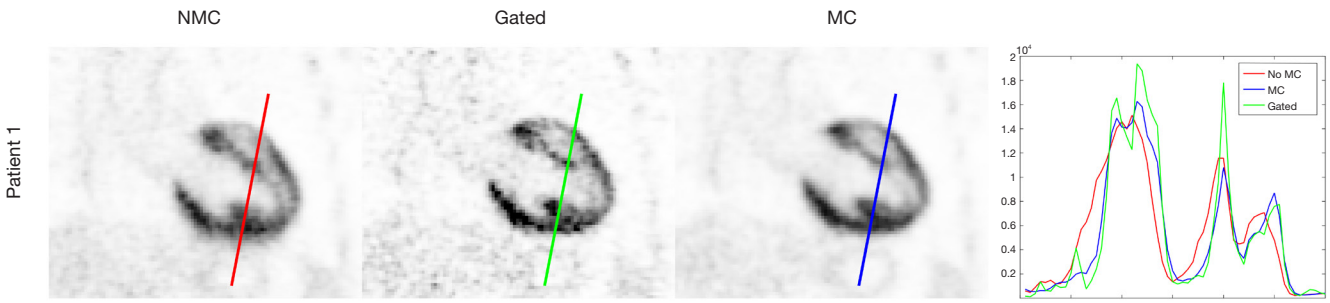

Figure 2 Cross-sectional images of the myocardium for an oncology patient showing images with non-motion correction (NMC), gated, and motion-corrected PET images, alongside with profiles across the myocardium. Motion correction improves the sharpness of the myocardium compared to NMC and reduces noise compared to gated images [Images reproduced with permission from Munoz *et al.* (94)].

compared to double-gated PET (3.2±0.9, P=0.04; 6±3, P=0.004). Küstner *et al.* used an MR self-navigation signal to train the respiratory signal which spanned the entire PET exam to serve as a more reliable respiratory motion estimate compared to the original respiratory signal from the external sensor. Using this method, the author reported an improvement of 22% in quantification and of 64% in delineation of malignant lesions on PET images after motion correction (95).

Imaging of carotid atherosclerosis

MRI

For a detailed description of identification of plaque composition with MRI and for expert recommendations on MRI protocols for carotid vessel wall imaging, we refer to a recent white paper (26). The main components of plaque vulnerability can be identified using a combination of different MRI contrasts (96-99). *Figure 3* shows an example of multi-contrast MRI of a patient with a carotid plaque. IPH is rich in methemoglobin which acts as an intrinsic T_1 relaxation time shortening agent, so that IPH appears bright when visualized with a hyper T_1 weighted (T_1w) sequence (*Figure 3A*) such as a three-dimensional magnetization-prepared rapid acquisition gradient echo (MP-RAGE) sequence (96,100-102). A comparison between the performance of different T_1w sequences [MP-RAGE, 3D TOF and 2D fast spin echo (2D-FSE)] demonstrated that MP-RAGE has the highest sensitivity and specificity for detecting IPH (103,104). Calcifications can be identified as regions with a hypointense signal in TOF, T_1w, proton

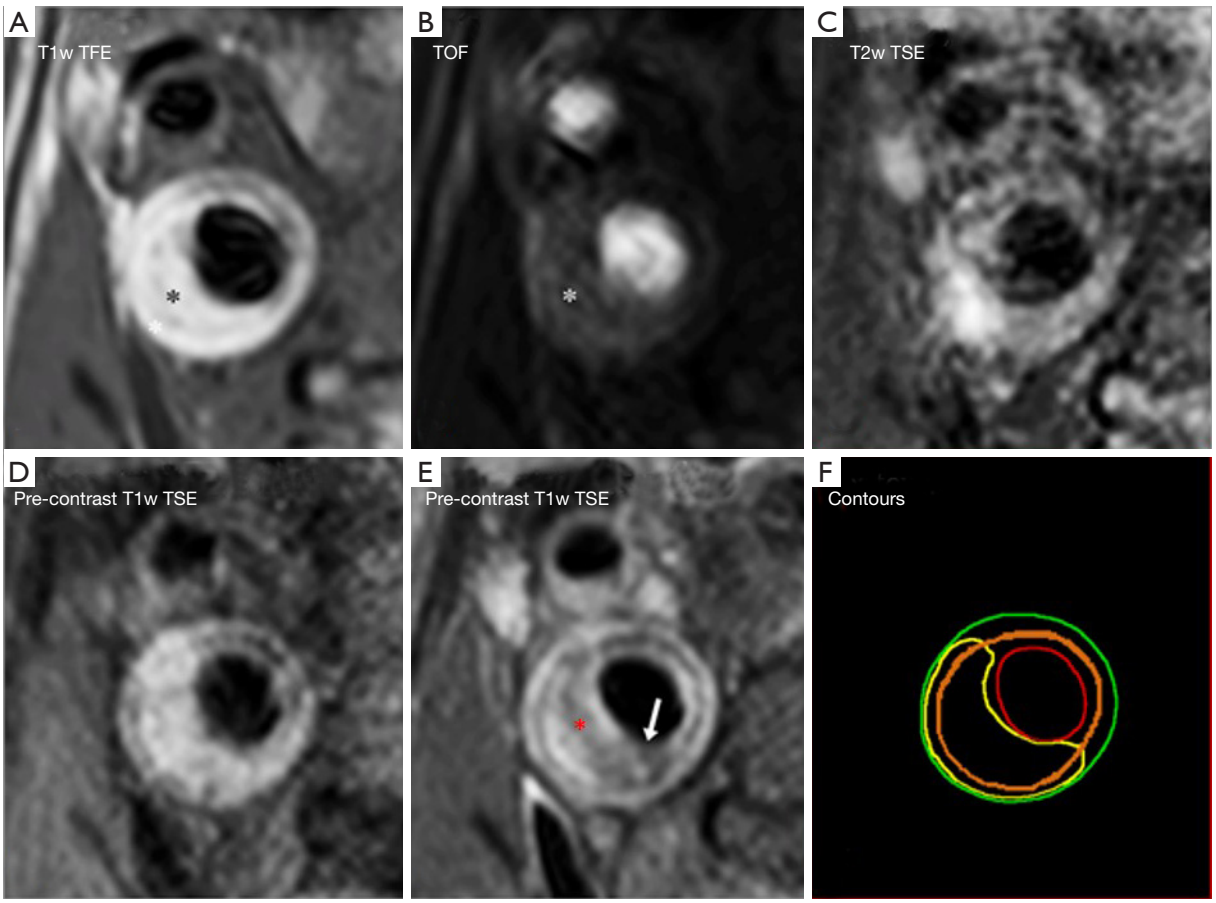

Figure 3 Co-registered (A) T1w TFE, (B) TOF, (C) T2w TSE, (D) pre- and (E) post-contrast T1w TSE images of a plaque in the internal carotid artery; (F) displays the delineation of plaque components and the inner and outer vessel wall: red = lumen; green = outer vessel wall; yellow = LRNC; orange = ring of calcifications; remaining vessel wall area = fibrous tissue. Hyperintense signal in A, and high signal in B (with respect to surrounding muscle tissue) in the bulk of the plaque is indicative for IPH (asterisk in T1w TFE and TOF images). A ring of hypointense signal, indicative for calcifications, is observed in all weightings [orange in (F)]. The lipid-rich necrotic core (yellow contour) can be identified as a region within the bulk of the plaque which does not enhance on black blood T1w MRI [red asterisk in (E)]. The fibrous cap can be recognized as a region with signal enhancement on the post-contrast images between the lipid-rich necrotic core and the lumen. This region with enhancement is interrupted, indicating a thin or ruptured fibrous cap [arrow in (E)]. [Images reproduced with permission from Kwee *et al.* (22)].

density weighted (PDW) and T_2w images (*Figure 3D*) (105). LRNC is characterized as a region within the bulk of the plaque that does not enhance on black blood T_1w contrast-enhanced MR images (CE-MRI) (*Figure 3E*) (106). The fibrous cap is scored as thick, when a continuous region with contrast enhancement separates the LRNC from the lumen. When the LRNC extends to the lumen, fibrous cap is scored as thin or ruptured (*Figure 3E*) (107,108). CE-MRI improves the contrast between the LRNC and the fibrous cap (109). Neo-vascularization is another vulnerable plaque component which can be visualized using pharmacokinetic modeling of dynamic contrast-enhanced MRI (*Figure 4*) (111,112). Plaque burden (plaque volume normalized to the total vessel volume) requires high contrast between the plaque and the lumen, which can be achieved using black blood T_1w MRI sequences (113).

Currently, a carotid MRI exam to visualize different plaque components takes approximately 20–30 minutes. Multicontrast sequences allow the visualization of different vulnerable plaque components with a single acquisition and tremendously reduce scan time. One such sequence, simultaneous non-contrast angiography and intraplaque

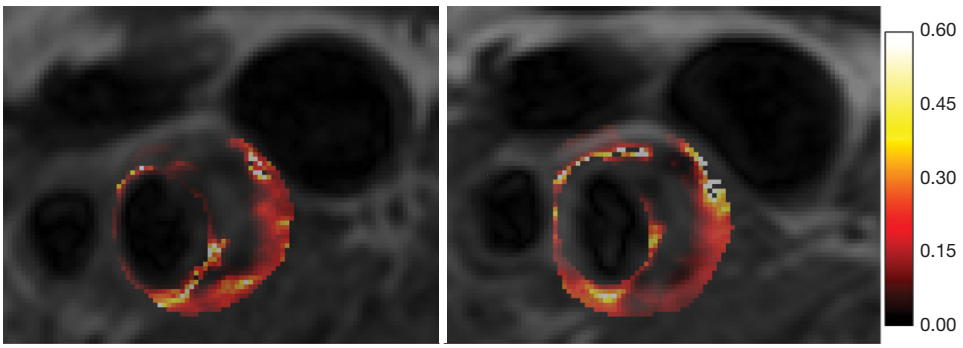

Figure 4 Maps generated from images acquired 1 week apart of a 70-year-old male. Parametric maps are overlaid on anatomic MR images, and voxel K^{trans} values which reflect microvascular flow, permeability, and surface area, are color coded from 0 to 0.6 min^{-1}. The parametric maps that are acquired on two different days are very similar indicating a high scan-rescan reproducibility. The necrotic core exhibits low K^{trans} values at the bulk of the plaque, while the highly vascularized adventitia at the outer rim demonstrates high K^{trans} values. Another region of higher K^{trans} values is observed near the inner rim of the plaque. [Reproduced, with permission, from Gaens *et al.* (110)].

hemorrhage (SNAP), acquires hyper T_1w black blood images and bright blood images with a single scan. Two separate studies of 13 and 54 patients with carotid plaques, compared the performance of SNAP with MP-RAGE and found that there was a moderate to very good agreement between the two sequences for the identification of IPH (κ=0.82, P=0.141 and κ=0.511, P=0.029, respectively), although the area of IPH detected by SNAP was significantly larger compared to MPRAGE in the latter study (17.9±18.2 *vs.* 9.2±10.5 mm^2, P<0.001). A large study comparing SNAP with histology as gold standard still needs to be carried out. The degree of stenosis on the SNAP bright blood images was significantly correlated with that measured by TOF MR angiography (intraclass correlation coefficient =0.96, P<0.001), but validation with a clinical gold standard such as contrast-enhanced MR angiography (CE-MRA) is still lacking (114,115).

Another multicontrast sequence, multi-contrast atherosclerosis characterization (MATCH) (116), acquires three different contrasts (hyper T_1w black blood, grey blood and T_2w black blood). In a study with 53 patients, MATCH showed results comparable to a conventional multicontrast protocol (TOF, T_1w, T_2w) in quantitative measures of luminal area, outer wall area, mean area of LRNC and loose matrix, while MATCH showed a larger mean area of IPH and calcifications. The performance of MATCH was not compared to a hyper T_1w sequence such as MP-RAGE. In the same study, using carotid endarterectomy specimens from 13 patients as a reference, MATCH performed as well as the conventional sequences (TOF, T_1w, T_2w) in detecting IPH, LRNC, loose matrix, and calcifications with an acquisition time of only 2 ½ minutes (117). MATCH needs to be validated with histology in larger studies.

PET

For detailed information on PET imaging of atherosclerosis, we refer to the following reviews (118-120). For imaging carotid atherosclerosis, 18-fluorodeoxyglucose (^{18}F-FDG), a glucose analog, is often used as a surrogate marker for inflammation (*Figure 5*) (121-123). ^{18}F-FDG is taken up non-specifically by all cells that consume glucose including skeletal muscles, which can cause hinderance in the visualization of tracer uptake in the vessel wall. Other tracers, including ^{64}Cu-DOTATATE (124), ^{68}Ga-DOTATOC (125), ^{18}F-Choline (126) and ^{68}Ga Pentixafor (127), which are more specific for plaque inflammation, have been explored, but still need to be validated in larger studies. 18-fluorine sodium fluoride (^{18}F-NaF) has been used to identify active calcification showing the potential to visualize micro-calcifications which are too small to be seen on MRI or CT (128,129). HX4 (130) is another tracer, used to target hypoxia.

Carotid PET/MRI patient studies

An overview of PET/MRI studies in patients with carotid and coronary artery disease is provided in *Table 1*. In carotid PET/MRI studies featured here, motion correction techniques were not utilized as carotid arteries are subject to only slight motion and five (124,127,133-135 of the seven studies used the Dixon sequence to create MR-based PET

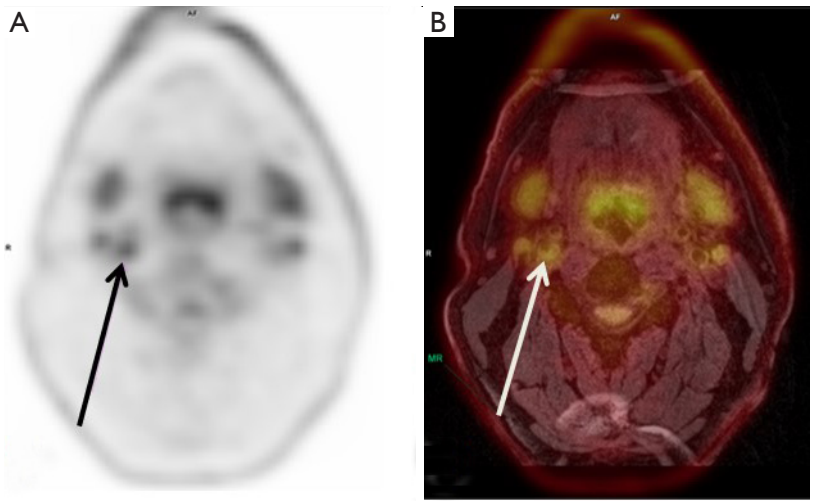

Figure 5 (A) ^{18}F-FDG PET image of the neck (left) of a patient with a carotid plaque; (B) a colour overlay of the PET image as displayed in (A) on the corresponding MR image. Anatomical information from MRI confirms ^{18}F FDG uptake in the symptomatic carotid plaque (arrow), while hardly any uptake is shown in the contralateral asymptomatic carotid artery.

attenuation maps. Fernandez-Friera *et al.* (131) quantified vascular inflammation using ^{18}F-FDG sequential PET/MRI in femoral, aorta, carotid and iliac arteries in 755 individuals with known plaques detected during pre-screening with ultrasound and CT. A free breathing, 3D T_1w spoiled gradient echo sequence was used for the whole-body MR-based attenuation maps using three tissue classifications (soft tissue, lung and air). PET/MRI facilitated the acquisition of T_1w and T_2w black blood MR images to visualize the vessel wall and to classify plaques as lipid-rich, fibrous or mixed. Arterial inflammation was scored qualitatively as increased vascular ^{18}F-FDG uptake by scoring the presence and number of locations with ^{18}F-FDG uptake. SUV_{max} and TBR_{max} values at these locations were calculated. Fused PET/MR images were used to determine which plaques showed inflammation (^{18}F-FDG uptake) and SUV_{max} and TBR_{max} was calculated for each plaque. The authors found arterial inflammation in 48.2% of the population and plaques on MRI in 90.1% of the population. Plaques with inflammation showed higher SUV_{max} and TBR_{max} values (P<0.001). They also reported that most uptake was found in plaque-free arterial segments on MRI (61.5%), suggesting arterial inflammation may be a precursor of atherosclerosis.

Bachi *et al.* (132) used ^{18}F-FDG simultaneous PET/MRI to assess carotid inflammation and plaque burden in individuals with cocaine use disorder (iCUD), healthy volunteers and individuals with cardiovascular risk factors. TOF MRI was acquired to delineate the vessel lumen. A 3D SPACE sequence was used to acquire black blood images to quantify lumen, wall area and wall thickness. PET attenuation was corrected using a template-based method. The authors showed that iCUD and healthy controls showed mild to moderate plaque inflammation (1.6> TBR <3), whereas the iCUD group showed the thickest carotid vessel wall.

Hyafil *et al.* (133) evaluated the morphological and functional features of non-stenotic carotid lesions in patients with cryptogenic stroke using ^{18}F-FDG simultaneous PET/MRI. The MRI sequence protocol included 3D TOF angiography, T_2w and pre- and post-contrast T_1w sequences. The prevalence of complicated plaques on MRI (AHA lesion type VI) was significantly higher in the ipsilateral carotid artery as compared to the contralateral side (39% *vs.* 0%; P=0.001), indicating that the plaque type was related to the clinical symptoms. Complicated atherosclerotic plaques were associated with higher ^{18}F-FDG uptake (TBR =3.43±1.13 *vs.* 2.41±0.84, P<0.001).

Pedersen *et al.* (124) demonstrated the feasibility of ^{64}Cu-DOTATATE as a molecular tracer of atherosclerotic plaque activity using simultaneous PET/MRI. To determine arterial wall thickness T_1w, T_2w and PDW MRI was acquired while TOF images were used to visualize luminal stenosis. SUV_{mean} values were calculated to quantify tracer uptake. The authors showed that the uptake correlated

Table 1 Description of patient studies on plaque imaging with PET/MRI

Reference	Subjects	Study aim	Main outcome
Friera *et al.* (131) (femoral, aorta, carotid and iliac)	755 patients with subclinical atherosclerosis	Characterize multi-territorial vascular inflammation using ^{18}F-FDG PET/MRI	Arterial inflammation was present in 48.2% of the individuals. ^{18}F-FDG uptake was present in 11% of the plaques that were detected on MRI, and in 61.5% of the plaque free arterial segments
Bachi *et al.* (132) (carotid)	10 individuals with cocaine use disorder (iCUD), 14 healthy control and 62 individuals with cardiovascular risk factors	Assess inflammation and plaque burden in iCUD using ^{18}F-FDG PET/MRI	iCUD and healthy controls showed mild to moderate plaque inflammation (1.6> TBR <3). The cardiovascular risk group did not undergo a PET scan. Using MRI, iCUD group showed significantly thicker carotid vessel walls compared to the cardiovascular risk group (P=0.001) and the healthy control group (P=0.005)
Hyafil *et al.* (133) (carotid)	18 patients with ischemic stroke classified as cryptogenic and presenting with non-stenotic carotid atherosclerotic plaques	Evaluate the morphological and functional features of atherosclerotic plaques in non-stenotic carotid lesions using ^{18}F-FDG PET/MRI	Prevalence of complicated atherosclerotic plaques (AHA lesion type VI) was significantly higher in the ipsilateral carotid artery as compared to the contralateral side (39% *vs.* 0%; P=0.001). Complicated atherosclerotic plaques were associated with higher ^{18}F-FDG uptake (TBR =3.43±1.13 *vs.* 2.41±0.84, P<0.001)
Pedersen *et al.* (124) (carotid)	10 TIA or stroke patients scheduled for carotid endarterectomy	Evaluate ^{64}Cu-DOTATATE as an *in-vivo* molecular tracer of atherosclerotic plaque activity	SUV_{mean} values were significantly higher in the ipsilateral lesion compared to the contralateral lesion (13.1% higher in ipsilateral plaques; P<0.001). No correlation was found between ^{64}Cu-DOTATATE uptake and plaque burden on MRI (P=0.116)
Li *et al.* (127) (carotid artery, aortic arch, ascending and descending aorta, and abdominal aorta)	38 oncology patients with focal arterial uptake of [^{68}Ga] Pentixafor	Evaluate the relation between CXCR4 expression and cardiovascular risk profile of the patients and determine the reproducibility of [^{68}Ga] Pentixafor uptake quantification of atherosclerotic lesions with PET/MRI	The tracer showed high arterial uptake (TBR_{max} >1.7) in patients which showed cardiovascular risk factors with the mean TBR_{max} value of high-risk patients being significantly higher than patients at low cardiovascular risk (1.9±0.3 *vs.* 1.7±0.2, P<0.05). TBR_{max} uptake values of lesions obtained from the baseline and follow-up scans (111±38 days after baseline) showed a good correlation (r=0.6, P<0.01) and there was no significant difference in mean TBR_{max} values derived from corresponding lesions between the two examinations
Li *et al.* (134) (carotid)	34 patients with carotid atherosclerotic plaques	Evaluate the reliability and accuracy of ^{18}F-FDG PET/MRI uptake quantification compared to PET/CT as a reference standard	SUV_{max} values of carotid plaque lesions were significantly lower on PET/MRI than on PET/CT (2.3±0.6 *vs.* 3.1±0.6; P<0.01). There was a moderate correlation between PET/CT and PET/ MRI SUV_{max} values (Spearman's r=0.67, P<0.01). TBR_{max} values of plaque lesions were similar on PET/MRI and PET/CT (2.2±0.3 *vs.* 2.2±0.3; P=0.4). There was a good correlation of TBR_{max} values between PET/MRI and PET/CT (Spearman's r=0.73, P<0.01). In this study the patients were scanned first with PET/CT, followed by PET/MRI
Ripa *et al.* (135) (carotid)	6 HIV-positive men with increased risk of atherosclerosis but no symptoms of cardiovascular diseases	Compare PET/MRI to PET/CT for imaging the carotid arteries in patients with known increased risk of atherosclerosis using ^{18}F-FDG PET/MRI	Mean difference of SUV_{mean} and SUV_{max} on PET/MRI versus PET/CT was −0.18 (P<0.001) and −0.14 (P<0.001), respectively, showing small but significant lower values with the PET/MRI. The patients were scanned first with PET/MRI followed by PET/CT

Table 1 (*continued*)

Table 1 (*continued*)

Reference	Subjects	Study aim	Main outcome
Andrews *et al.* (136) (coronary arteries and aortic valve)	18 patients (7 with aortic stenosis and 11 with recent myocardial infarction)	To investigate whether quantification of tracer (^{18}F-fluoride) uptake in the aortic valve and coronary arteries differs between PET/CT and PET/MR (using both the Dixon and radial GRE attenuation correction approach)	Coronary artery TBR_{max} values were comparable, although slightly higher using GRE AC PET/MR (1.24±0.27) than PET/CT (1.09±0.19, P=0.03; 95% limits of agreement −54% to 31%) and Dixon AC PET/MR (1.09±0.26, P≥0.99; 95% limits of agreement = −41% to 42%)
Munoz *et al.* (94,137) (coronary)	The CMRA approach was studied in 10 healthy subjects and 5 patients with coronary artery disease underwent ^{18}F-FDG PET/MRI	Test the feasibility of motion-corrected whole heart simultaneous PET/MRI	The visible length of the right coronary artery and left anterior descending artery on the MR images increased by 45.53% and 75.45%, and mean sharpness by 56.44% and 51.11%, respectively, when applying the proposed technique compared to no motion correction. For PET images the proposed technique outperformed no motion correction in terms of noise and mean SUV and outperformed a gated approach in terms of noise

independently (P=0.031) with the CD163 positive macrophages. No correlation was found between ^{64}Cu-DOTATATE uptake and plaque burden as assessed on MRI (P=0.116).

Li *et al.* (127) used ^{68}Ga Pentixafor tracer which targets macrophages using simultaneous PET/MRI. TOF magnetic resonance angiography was performed for grading carotid luminal stenosis. The tracer showed high arterial uptake (TBR_{max} >1.7) in patients with cardiovascular risk factors with the mean TBR_{max} value of high-risk patients being significantly higher (TBR_{max}: 1.9±0.3 *vs.* 1.7±0.2, P<0.05 high versus low risk, respectively).

Li *et al.* (134) evaluated the reliability and accuracy of measuring ^{18}F-FDG uptake on PET/MRI compared to PET/CT in 34 patients with carotid atherosclerotic plaques. A moderate correlation between carotid SUV_{max} on PET/MRI versus PET/CT was observed (Spearman's r=0.67, P<0.01). The SUV_{max} was significantly lower on PET/MRI than on PET/CT (2.3±0.6 *vs.* 3.1±0.6; P<0.01). TBR_{max} of plaque lesions was similar on PET/MRI and on PET/CT (2.2±0.3 *vs.* 2.2±0.3; P=0.4) and showed a good mutual correlation (Spearman's r=0.73, P<0.01). In this study, the patients were scanned first with PET/CT, followed by PET/MRI.

Ripa *et al.* (135) compared simultaneous PET/MRI to PET/CT for imaging the carotid arteries in patients with increased risk of atherosclerosis using ^{18}F-FDG. 3D TOF MR angiography was performed to determine luminal stenosis. Dark blood T_1w, T_2w and proton density weightings were also acquired to visualize the arterial wall. They showed that the mean difference for SUV_{mean} and SUV_{max} was −0.18 (P<0.001) and −0.14 (P<0.001), respectively, showing small but significantly lower values with PET/MRI. In this study the patients underwent a PET/MRI first followed by a PET/CT.

Coronary vessel wall imaging

MRI

Several studies have shown the efficacy of coronary MR angiography (CMRA) to detect coronary artery stenosis (138-140). Due to the tortuous nature and constant movement of the coronary arteries, CMRA is usually performed with 3D sequences and respiratory motion compensation while gadolinium (Gd)-based contrast agents can be used to further improve blood to myocardium contrast for improved vessel visualization (141). Contrast-

enhanced coronary vessel wall imaging has been shown to be promising for the identification of the culprit lesion, since these lesions show pronounced contrast uptake in patients with acute myocardial infarction (142). Non-contrast black blood MRI has been used to visualize coronary vessel lumen and wall (143). High intensity signal (HIS) plaques can be identified on heavily T_1w MR images (144-146). This hyper intense signal is attributed to IPH and/or luminal thrombosis (144,145,147) and can be used as a predictor for adverse coronary events (hazard ratio: 3.96; 95% confidence interval: 1.92 to 8.17; P<0.001) (148). MRI sequences used to visualize coronary vessel wall have shortcomings such as incomplete coverage of the heart, poor anisotropic spatial resolution, and the requirement for an additional anatomic reference scan of the lumen that can lead to misregistration errors (149).

To counter these issues, multicontrast sequences have been developed for coronary artery imaging.

A novel sequence, coronary atherosclerosis T_1w characterization with integrated anatomical reference (CATCH), allows the acquisition of T_1w dark blood and anatomical reference bright blood images with a single sequence. Hyperintense plaques on CATCH images were positively associated with high risk plaque features on invasive angiography and optical coherence tomography (150).

Bright- and black-blood phase sensitive inversion recovery sequence (BOOST) is another multicontrast sequence for coronary plaque imaging that acquires bright and black blood images with a single sequence, employing preparation pulses to improve the contrast of anatomical reference bright blood images (151). The feasibility of thrombus visualization with BOOST was shown in an *ex-vivo* pig heart.

PET

The intrinsic low spatial resolution of PET combined with cardiac and respiratory motion, make coronary artery PET challenging. ^{18}F-FDG and ^{18}F-NaF have been used for the evaluation of atherosclerosis in the coronary arteries (152-154). The high myocardial uptake of ^{18}F-FDG can obscure coronary plaque inflammation. This uptake can be suppressed by consuming a high- fat low-carbohydrate diet and by fasting before the PET exam (155).

Coronary PET/MRI patient studies

Andrews *et al.* (136) investigated whether quantification of tracer (^{18}F-fluoride) uptake in the aortic valve and coronary arteries differs between PET/CT and simultaneous PET/MR (using both the Dixon and a novel free breathing radial gradient recalled echo (GRE) attenuation correction approach) in 18 patients with aortic stenosis or recent myocardial infarction. A free-breathing radial GRE attenuation correction map was generated (90). In non-stented patients, coronary artery TBR_{max} was comparable, although slightly higher using GRE attenuation correction PET/MR (1.24±0.27) than PET/CT (1.09±0.19, P=0.03) and Dixon attenuation correction PET/MR (1.09±0.26, P≥0.99).

Future developments

Until now, plaque imaging with PET/MRI has been focused on carotids and coronary arteries with ^{18}F-FDG as the most commonly used tracer. Other vascular beds such as intracranial and peripheral arteries provide opportunities that can be explored with PET/MRI. Novel PET tracers combined with MRI based PET motion correction is a major advantage of PET/MRI. With PET tracers that specifically target particular vulnerable plaque features, motion-corrected PET images ensure increased sensitivity. MR based PET motion correction could help realize the full potential of PET imaging. RF-coils also need to be updated. Coils designed specifically to minimize photon attenuation caused by the coil while maintaining if not improving MR image quality could be the answer to using flexible RF-coils in PET/MRI.

Radiomics is a rapidly growing field which essentially involves extraction of comprehensive quantitative features such shape, size, volume, signal intensity and texture of the ROI. By combining PET with different MRI contrasts, features from the two modalities can be derived, which increase the chance to detect subtle differences in the radiological images which cannot be visualized by human observers. Currently, radiomic feature extraction from PET/MRI is being implemented more in the field of oncology such as for texture analysis from combined PET and CE-MRI to differentiate radiation injury from recurrent brain metastasis (156), to predict recurrence of cervical cancer in patients (157), or to characterize early treatment response in renal cancer (158). PET/MRI based radiomics could aid in risk stratification, evaluation of treatment response and provide new insights into plaque development.

The latest developments in deep learning applications for hybrid imaging are reviewed by Zaharchuk *et al.* (159). We have already described how deep learning can be used to create PET attenuation maps. Currently, artificially

intelligence is being used to denoise images (160), reconstruct MR images with undersampled data (161), image segmentation (162), reduce PET dose (163-165) and predict PET images based solely on MR image input (166). Moving forward, we may expect to see autonomous systems that use PET/MR images to calculate a risk score and act as an assistant to the physician.

Conclusions

Although they are still costly and availability is limited, the clinical acceptance of PET/MRI and the number of installed systems is steadily rising. The combination of superior soft tissue contrast of MRI with molecular imaging by PET and relatively lower radiation dose make hybrid PET/MRI well suited for evaluation of new drugs, therapy monitoring, to gain more insights into factors that contribute to plaque progression and destabilization and for patient risk stratification. Due to its simultaneous nature, the inherent co-registration of the two modalities is superior to other hybrid imaging modalities currently available. This also enables MR-based motion correction of PET data, another advantage of PET/MRI. MR-based attenuation correction algorithms are considered sufficient, at least for clinical interpretation of the images. Additionally, new developments such as PET lucent coils, new reconstruction algorithms such as compressed sensing and deep learning based low-dose PET reconstructions have the potential to improve image quality, reduce scan times, reduce radiation dose and overall improve patient comfort. Concluding, PET/MRI has the potential to become a one stop shop modality for patients with atherosclerosis, but further validation in larger clinical studies is warranted.

Acknowledgments

We thank Dr. Camila Munoz for providing images used in this publication.
Funding: The authors acknowledge the financial support provided by European Union's Horizon 2020 research and innovation program under the Marie Skłodowska-Curie grant agreement No. 722609. MEK is supported by an Aspasia Grant 015.014.010 from The Netherlands Organization for Scientific Research.

Footnote

Provenance and Peer Review: This article was commissioned by the Guest Editor (Luca Saba) for the series "Advanced Imaging in The Diagnosis of Cardiovascular Diseases" published in *Cardiovascular Diagnosis and Therapy*. The article was sent for external peer review organized by the Guest Editor and the editorial office.

Conflicts of Interest: All authors have completed the ICMJE uniform disclosure form (available at http://dx.doi.org/10.21037/cdt.2020.02.09). The series "Advanced Imaging in The Diagnosis of Cardiovascular Diseases" was commissioned by the editorial office without any funding or sponsorship. Dr. RPMM reports grants from Stichting de Weijerhorst, outside the submitted work; Prof. Dr. MEK reports grants from European Union's Horizon 2020 research and innovation program under the Marie Skłodowska-Curie grant agreement No. 722609 and a grant from NWO/ASPASIA, during the conduct of the study; grant from Stichting De Weijerhorst, grant from NWO Hestia, outside the submitted work. The other authors have no conflicts of interest to declare.

Ethical Statement: The authors are accountable for all aspects of the work in ensuring that questions related to the accuracy and integrity of any part of the work are appropriately investigated and resolved.

References

1. Lusis AJ. Atherosclerosis. Nature 2000;407:233-41.
2. World Health Organization. Cardiovascular diseases (CVDs). 2017. Available online: http://www.who.int/news-room/fact-sheets/detail/cardiovascular-diseases-(cvds). Accessed 4 Sep 2019.
3. Benjamin EJ BM, Chiuve SE, Cushman M, et al. Heart Disease and Stroke Statistics 2017 At a Glance. 2017.
4. Goldbourt U, Neufeld HN. Genetic aspects of arteriosclerosis. Arteriosclerosis 1986;6:357-77.
5. Assmann G, Cullen P, Jossa F, et al. Coronary Heart

Disease: Reducing the Risk. Arterioscler Thromb Vasc Biol 1999;19:1819-24.
6. Cunningham KS, Gotlieb AI. The role of shear stress in the pathogenesis of atherosclerosis. Lab Invest 2005;85:9-23.
7. Traub O, Berk BC. Laminar shear stress - Mechanisms by which endothelial cells transduce an atheroprotective force. Arterioscler Thromb Vasc Biol 1998;18:677-85.
8. Libby P. Inflammation in atherosclerosis. Nature 2002;420:868-74.
9. Sluimer JC, Daemen MJ. Novel concepts in atherogenesis: angiogenesis and hypoxia in atherosclerosis. J Pathol 2009;218:7-29.
10. Sluimer JC, Gasc JM, van Wanroij JL, et al. Hypoxia, hypoxia-inducible transcription factor, and macrophages in human atherosclerotic plaques are correlated with intraplaque angiogenesis. J Am Coll Cardiol 2008;51:1258-65.
11. Parma L, Baganha F, Quax PHA, et al. Plaque angiogenesis and intraplaque hemorrhage in atherosclerosis. Eur J Pharmacol 2017;816:107-15.
12. Crombag GA, Schreuder F, van Hoof RHM, et al. Microvasculature and intraplaque hemorrhage in atherosclerotic carotid lesions: a cardiovascular magnetic resonance imaging study. J Cardiovasc Magn Reson 2019;21:15.
13. New SE, Goettsch C, Aikawa M, et al. Macrophage-derived matrix vesicles: an alternative novel mechanism for microcalcification in atherosclerotic plaques. Circ Res 2013;113:72-7.
14. Kapustin AN, Davies JD, Reynolds JL, et al. Calcium regulates key components of vascular smooth muscle cell-derived matrix vesicles to enhance mineralization. Circ Res 2011;109:e1-12.
15. Vancraeynest D, Pasquet A, Roelants V, et al. Imaging the vulnerable plaque. J Am Coll Cardiol 2011;57:1961-79.
16. Virmani R, Kolodgie FD, Burke AP, et al. Lessons from sudden coronary death - A comprehensive morphological classification scheme for atherosclerotic lesions. Arterioscler Thromb Vasc Biol 2000;20:1262-75.
17. Ammirati E, Moroni F, Norata GD, et al. Markers of inflammation associated with plaque progression and instability in patients with carotid atherosclerosis. Mediators Inflamm 2015;2015:718329.
18. Matz O, Nikoubashman O, Rajkumar P, et al. Grading of proximal internal carotid artery (ICA) stenosis by Doppler/duplex ultrasound (DUS) and computed tomographic angiography (CTA): correlation and interrater reliability in real-life practice. Acta Neurol Belg 2017;117:183-8.
19. Rothwell PM, Eliasziw M, Gutnikov SA, et al. Endarterectomy for symptomatic carotid stenosis in relation to clinical subgroups and timing of surgery. Lancet 2004;363:915-24.
20. Schindler A, Schinner R, Altaf N, et al. Prediction of Stroke Risk by Detection of Hemorrhage in Carotid Plaques: Meta-Analysis of Individual Patient Data. JACC Cardiovasc Imaging 2020;13:395-406.
21. Kelly PJ, Camps-Renom P, Giannotti N, et al. Carotid Plaque Inflammation Imaged by (18)F-Fluorodeoxyglucose Positron Emission Tomography and Risk of Early Recurrent Stroke. Stroke 2019;50:1766-73.
22. Kwee RM, van Oostenbrugge RJ, Mess WH, et al. MRI of carotid atherosclerosis to identify TIA and stroke patients who are at risk of a recurrence. J Magn Reson Imaging 2013;37:1189-94.
23. Gupta A, Baradaran H, Schweitzer AD, et al. Carotid plaque MRI and stroke risk: a systematic review and meta-analysis. Stroke 2013;44:3071-7.
24. Kwee RM, van Oostenbrugge RJ, Hofstra L, et al. Identifying vulnerable carotid plaques by noninvasive imaging. Neurology 2008;70:2401-9.
25. Daghem M, Bing R, Fayad ZA, et al. Noninvasive Imaging to Assess Atherosclerotic Plaque Composition and Disease Activity: Coronary and Carotid Applications. JACC Cardiovasc Imaging 2020;13:1055-68.
26. Saba L, Yuan C, Hatsukami TS, et al. Carotid Artery Wall Imaging: Perspective and Guidelines from the ASNR Vessel Wall Imaging Study Group and Expert Consensus Recommendations of the American Society of Neuroradiology. AJNR Am J Neuroradiol 2018;39:E9-31.
27. Marnane M, Merwick A, Sheehan OC, et al. Carotid plaque inflammation on 18F-fluorodeoxyglucose positron emission tomography predicts early stroke recurrence. Ann Neurol 2012;71:709-18.
28. van Geuns RJ, Wielopolski PA, de Bruin HG, et al. Basic principles of magnetic resonance imaging. Prog Cardiovasc Dis 1999;42:149-56.
29. Saha GB. Data Acquisition and Corrections. In: Basics of PET Imaging. Cham: Springer, 2016.
30. Tarkin JM, Joshi FR, Rudd JH. PET imaging of inflammation in atherosclerosis. Nat Rev Cardiol 2014;11:443-57.
31. Bailey DL, Karp JS, Surti S. Physics and Instrumentation in PET. In: Bailey DL, Townsend DW, Valk PE, et al. editors. Positron Emission Tomography. London: Springer, 2005:13-39.
32. Conti M, Bendriem B. The new opportunities for high time resolution clinical TOF PET. Clin Transl Imaging

2019;7:139-47.
33. Torigian DA, Zaidi H, Kwee TC, et al. PET/MR imaging: technical aspects and potential clinical applications. Radiology 2013;267:26-44.
34. Jung JH, Choi Y, Im KC. PET/MRI: Technical Challenges and Recent Advances. Nucl Med Mol Imaging 2016;50:3-12.
35. Shah SN, Huang SS. Hybrid PET/MR imaging: physics and technical considerations. Abdom Imaging 2015;40:1358-65.
36. Wagenknecht G, Kaiser HJ, Mottaghy FM, et al. MRI for attenuation correction in PET: methods and challenges. MAGMA 2013;26:99-113.
37. Zaidi H, Ojha N, Morich M, et al. Design and performance evaluation of a whole-body Ingenuity TF PET-MRI system. Phys Med Biol 2011;56:3091-106.
38. Jadvar H, Colletti PM. Competitive advantage of PET/MRI. Eur J Radiol 2014;83:84-94.
39. Beyer T, Schwenzer N, Bisdas S, et al. MR/PET – Hybrid Imaging for the Next Decade. MAGNETOM Flash 2010;3:19-29.
40. SIGNA™ PET/MR with QuantWorks – 60cm. Available online: https://www.gehealthcare.com/products/magnetic-resonance-imaging/3-0t/signa-pet-mr. Accessed 26 Sep 2019.
41. Herzog H, Lerche C. Advances in Clinical PET/MRI Instrumentation. PET Clin 2016;11:95-103.
42. Mehranian A, Arabi H, Zaidi H. Quantitative analysis of MRI-guided attenuation correction techniques in time-of-flight brain PET/MRI. Neuroimage 2016;130:123-33.
43. Burger C, Goerres G, Schoenes S, et al. PET attenuation coefficients from CT images: experimental evaluation of the transformation of CT into PET 511-keV attenuation coefficients. Eur J Nucl Med Mol Imaging 2002;29:922-7.
44. Coombs BD, Szumowski J, Coshow W. Two-point Dixon technique for water-fat signal decomposition with B0 inhomogeneity correction. Magn Reson Med 1997;38:884-9.
45. Aasheim LB, Karlberg A, Goa PE, et al. PET/MR brain imaging: evaluation of clinical UTE-based attenuation correction. Eur J Nucl Med Mol Imaging 2015;42:1439-46.
46. Sekine T, Ter Voert EE, Warnock G, et al. Clinical Evaluation of Zero-Echo-Time Attenuation Correction for Brain 18F-FDG PET/MRI: Comparison with Atlas Attenuation Correction. J Nucl Med 2016;57:1927-32.
47. Blumhagen JO, Ladebeck R, Fenchel M, et al. MR-based field-of-view extension in MR/PET: B0 homogenization using gradient enhancement (HUGE). Magn Reson Med 2013;70:1047-57.
48. Blumhagen JO, Braun H, Ladebeck R, et al. Field of view extension and truncation correction for MR-based human attenuation correction in simultaneous MR/PET imaging. Med Phys 2014;41:022303.
49. Schreibmann E, Nye JA, Schuster DM, et al. MR-based attenuation correction for hybrid PET-MR brain imaging systems using deformable image registration. Med Phys 2010;37:2101-9.
50. Nuyts J, Dupont P, Stroobants S, et al. Simultaneous maximum a posteriori reconstruction of attenuation and activity distributions from emission sinograms. IEEE Trans Med Imaging 1999;18:393-403.
51. Han X. MR-based synthetic CT generation using a deep convolutional neural network method. Med Phys 2017;44:1408-19.
52. Nie D, Cao X, Gao Y, et al. Estimating CT Image from MRI Data Using 3D Fully Convolutional Networks. Deep Learn Data Label Med Appl (2016) 2016;2016:170-8.
53. Spuhler KD, Gardus J 3rd, Gao Y, et al. Synthesis of Patient-Specific Transmission Data for PET Attenuation Correction for PET/MRI Neuroimaging Using a Convolutional Neural Network. J Nucl Med 2019;60:555-60.
54. Shiri I, Ghafarian P, Geramifar P, et al. Direct attenuation correction of brain PET images using only emission data via a deep convolutional encoder-decoder (Deep-DAC). Eur Radiol 2019;29:6867-79.
55. Hwang D, Kang SK, Kim KY, et al. Generation of PET Attenuation Map for Whole-Body Time-of-Flight (18) F-FDG PET/MRI Using a Deep Neural Network Trained with Simultaneously Reconstructed Activity and Attenuation Maps. J Nucl Med 2019;60:1183-9.
56. Arabi H, Zeng G, Zheng G, et al. Novel adversarial semantic structure deep learning for MRI-guided attenuation correction in brain PET/MRI. Eur J Nucl Med Mol Imaging 2019;46:2746-59.
57. Leynes AP, Yang J, Wiesinger F, et al. Zero-Echo-Time and Dixon Deep Pseudo-CT (ZeDD CT): Direct Generation of Pseudo-CT Images for Pelvic PET/MRI Attenuation Correction Using Deep Convolutional Neural Networks with Multiparametric MRI. J Nucl Med 2018;59:852-8.
58. Ladefoged CN, Marner L, Hindsholm A, et al. Deep Learning Based Attenuation Correction of PET/MRI in Pediatric Brain Tumor Patients: Evaluation in a Clinical Setting. Front Neurosci 2019;12:1005.
59. Martinez-Möller A, Souvatzoglou M, Delso G, et al. Tissue classification as a potential approach for attenuation correction in whole-body PET/MRI: evaluation with PET/CT data. J Nucl Med 2009;50:520-6.
60. Attenberger U, Catana C, Chandarana H, et al. Whole-body FDG PET-MR oncologic imaging: pitfalls in clinical

interpretation related to inaccurate MR-based attenuation correction. Abdom Imaging 2015;40:1374-86.
61. Eldib M, Bini J, Calcagno C, et al. Attenuation Correction for Flexible Magnetic Resonance Coils in Combined Magnetic Resonance/Positron Emission Tomography Imaging. Invest Radiol 2014;49:63-9.
62. Sander CY, Keil B, Chonde DB, et al. A 31-channel MR brain array coil compatible with positron emission tomography. Magn Reson Med 2015;73:2363-75.
63. Aizaz SMM, Moonen RPM, Wierts R, et al. Evaluation of Attenuation Reduction of a Dedicated Carotid Pet/Mri Coil for Carotid Plaque Imaging. Atherosclerosis 2019;287:E51-2.
64. Ryan JL, Aaron VD, Sims JB. PET/MRI vs PET/CT in Head and Neck Imaging: When, Why, and How? Semin Ultrasound CT MR 2019;40:376-90.
65. Afaq A, Fraioli F, Sidhu H, et al. Comparison of PET/MRI With PET/CT in the Evaluation of Disease Status in Lymphoma. Clin Nucl Med 2017;42:e1-7.
66. Varoquaux A, Rager O, Poncet A, et al. Detection and quantification of focal uptake in head and neck tumours: (18)F-FDG PET/MR versus PET/CT. Eur J Nucl Med Mol Imaging 2014;41:462-75.
67. Drzezga A, Souvatzoglou M, Eiber M, et al. First clinical experience with integrated whole-body PET/MR: comparison to PET/CT in patients with oncologic diagnoses. J Nucl Med 2012;53:845-55.
68. Al-Nabhani KZ, Syed R, Michopoulou S, et al. Qualitative and quantitative comparison of PET/CT and PET/MR imaging in clinical practice. J Nucl Med 2014;55:88-94.
69. Schleyer PJ, Schaeffter T, Marsden PK. The effect of inaccurate bone attenuation coefficient and segmentation on reconstructed PET images. Nucl Med Commun 2010;31:708-16.
70. Delso G, Martinez-Moller A, Bundschuh RA, et al. The effect of limited MR field of view in MR/PET attenuation correction. Med Phys 2010;37:2804-12.
71. van Heeswijk RB, Bonanno G, Coppo S, et al. Motion compensation strategies in magnetic resonance imaging. Crit Rev Biomed Eng 2012;40:99-119.
72. Catana C. Motion correction options in PET/MRI. Semin Nucl Med 2015;45:212-23.
73. Henningsson M, Botnar RM. Advanced respiratory motion compensation for coronary MR angiography. Sensors (Basel) 2013;13:6882-99.
74. Munoz C, Kolbitsch C, Reader AJ, et al. MR-Based Cardiac and Respiratory Motion-Compensation Techniques for PET-MR Imaging. PET Clin 2016;11:179-91.
75. Scott AD, Keegan J, Firmin DN. Motion in cardiovascular MR imaging. Radiology 2009;250:331-51.
76. Ehman RL, McNamara MT, Pallack M, et al. Magnetic resonance imaging with respiratory gating: techniques and advantages. AJR Am J Roentgenol 1984;143:1175-82.
77. Fischer RW, Botnar RM, Nehrke K, et al. Analysis of residual coronary artery motion for breath hold and navigator approaches using real-time coronary MRI. Magn Reson Med 2006;55:612-8.
78. Stehning C, Bornert P, Nehrke K, et al. Free-breathing whole-heart coronary MRA with 3D radial SSFP and self-navigated image reconstruction. Magn Reson Med 2005;54:476-80.
79. Henningsson M, Koken P, Stehning C, et al. Whole-heart coronary MR angiography with 2D self-navigated image reconstruction. Magn Reson Med 2012;67:437-45.
80. Addy NO, Ingle RR, Luo J, et al. 3D image-based navigators for coronary MR angiography. Magn Reson Med 2017;77:1874-83.
81. Wu HH, Gurney PT, Hu BS, et al. Free-breathing multiphase whole-heart coronary MR angiography using image-based navigators and three-dimensional cones imaging. Magn Reson Med 2013;69:1083-93.
82. Bhat H, Ge L, Nielles-Vallespin S, et al. 3D radial sampling and 3D affine transform-based respiratory motion correction technique for free-breathing whole-heart coronary MRA with 100% imaging efficiency. Magn Reson Med 2011;65:1269-77.
83. Cruz G, Atkinson D, Henningsson M, et al. Highly efficient nonrigid motion-corrected 3D whole-heart coronary vessel wall imaging. Magn Reson Med 2017;77:1894-908.
84. Henningsson M, Prieto C, Chiribiri A, et al. Whole-heart coronary MRA with 3D affine motion correction using 3D image-based navigation. Magn Reson Med 2014;71:173-81.
85. Correia T, Ginami G, Cruz G, et al. Optimized respiratory-resolved motion-compensated 3D Cartesian coronary MR angiography. Magn Reson Med 2018;80:2618-29.
86. Feng L, Axel L, Chandarana H, et al. XD-GRASP: Golden-angle radial MRI with reconstruction of extra motion-state dimensions using compressed sensing. Magn Reson Med 2016;75:775-88.
87. Coppo S, Piccini D, Bonanno G, et al. Free-running 4D whole-heart self-navigated golden angle MRI: Initial results. Magn Reson Med 2015;74:1306-16.
88. Yerly J, Ginami G, Nordio G, et al. Coronary endothelial function assessment using self-gated cardiac cine MRI and k-t sparse SENSE. Magn Reson Med 2016;76:1443-54.

89. Bonanno G, Hays AG, Weiss RG, et al. Self-gated golden angle spiral cine MRI for coronary endothelial function assessment. Magn Reson Med 2018;80:560-70.
90. Robson PM, Trivieri M, Karakatsanis NA, et al. Correction of respiratory and cardiac motion in cardiac PET/MR using MR-based motion modeling. Phys Med Biol 2018;63:225011.
91. Picard Y, Thompson CJ. Motion correction of PET images using multiple acquisition frames. IEEE Trans Med Imaging 1997;16:137-44.
92. Petibon Y, El Fakhri G, Nezafat R, et al. Towards coronary plaque imaging using simultaneous PET-MR: a simulation study. Phys Med Biol 2014;59:1203-22.
93. Lamare F, Carbayo MJL, Cresson T, et al. List-mode-based reconstruction for respiratory motion correction in PET using non-rigid body transformations. Physics in Medicine and Biology 2007;52:5187-204.
94. Munoz C, Neji R, Cruz G, et al. Motion-corrected simultaneous cardiac positron emission tomography and coronary MR angiography with high acquisition efficiency. Magn Reson Med 2018;79:339-50.
95. Küstner T, Schwartz M, Martirosian P, et al. MR-based respiratory and cardiac motion correction for PET imaging. Med Image Anal 2017;42:129-44.
96. Yuan C, Oikawa M, Miller Z, et al. MRI of Carotid Atherosclerosis. J Nucl Cardiol 2008;15:266-75.
97. Yuan C, Mitsumori LM, Beach KW, et al. Carotid atherosclerotic plaque: noninvasive MR characterization and identification of vulnerable lesions. Radiology 2001;221:285-99.
98. Yuan C, Mitsumori LM, Ferguson MS, et al. In vivo accuracy of multispectral magnetic resonance imaging for identifying lipid-rich necrotic cores and intraplaque hemorrhage in advanced human carotid plaques. Circulation 2001;104:2051-6.
99. Cappendijk VC, Cleutjens KBJM, Kessels AGH, et al. Assessment of human atherosclerotic carotid plaque components with multisequence MR imaging: Initial experience. Radiology 2005;234:487-92.
100. McNally JS, Kim SE, Mendes J, et al. Magnetic Resonance Imaging Detection of Intraplaque Hemorrhage. Magn Reson Insights 2017;10:1-8.
101. Liu J, Balu N, Hippe DS, et al. Semi-automatic carotid intraplaque hemorrhage detection and quantification on Magnetization-Prepared Rapid Acquisition Gradient-Echo (MP-RAGE) with optimized threshold selection. J Cardiovasc Magn Reson 2016;18:41.
102. Mugler JP. Rapid three-dimensional T1-weighted MR imaging with the MP-RAGE sequence. JMRI 1991;1:561-7.
103. Ota H, Yarnykh VL, Ferguson MS, et al. Carotid Intraplaque Hemorrhage Imaging at 3.0-T MR Imaging: Comparison of the Diagnostic Performance of Three T1-weighted Sequences. Radiology 2010;254:551-63.
104. Cappendijk VC, Cleutjens KB, Heeneman S, et al. In vivo detection of hemorrhage in human atherosclerotic plaques with magnetic resonance imaging. J Magn Reson Imaging 2004;20:105-10.
105. Saam T, Ferguson MS, Yarnykh VL, et al. Quantitative evaluation of carotid plaque composition by in vivo MRI. Arterioscler Thromb Vasc Biol 2005;25:234-9.
106. Fitzpatrick LA, Berkovitz N, Dos Santos MP, et al. Vulnerable carotid plaque imaging and histopathology without a dedicated MRI receiver coil. Neuroradiol J 2017;30:120-8.
107. Hatsukami TS, Ross R, Polissar NL, et al. Visualization of fibrous cap thickness and rupture in human atherosclerotic carotid plaque in vivo with high-resolution magnetic resonance imaging. Circulation 2000;102:959-64.
108. Kwee RM, van Engelshoven JMA, Mess WH, et al. Reproducibility of Fibrous Cap Status Assessment of Carotid Artery Plaques by Contrast-Enhanced MRI. Stroke 2009;40:3017-21.
109. Wasserman BA, Casal SG, Astor BC, et al. Wash-in kinetics for gadolinium-enhanced magnetic resonance imaging of carotid atheroma. J Magn Reson Imaging 2005;21:91-5.
110. Gaens ME, Backes WH, Rozel S, et al. Dynamic contrast-enhanced MR imaging of carotid atherosclerotic plaque: model selection, reproducibility, and validation. Radiology 2013;266:271-9.
111. van Hoof RH, Heeneman S, Wildberger JE, et al. Dynamic Contrast-Enhanced MRI to Study Atherosclerotic Plaque Microvasculature. Curr Atheroscler Rep 2016;18:33.
112. Kerwin W, Hooker A, Spilker M, et al. Quantitative magnetic resonance imaging analysis of neovasculature volume in carotid atherosclerotic plaque. Circulation 2003;107:851-6.
113. Kerwin WS, Hatsukami T, Yuan C, et al. MRI of carotid atherosclerosis. AJR Am J Roentgenol 2013;200:W304-13.
114. Li D, Zhao H, Chen X, et al. Identification of intraplaque haemorrhage in carotid artery by simultaneous non-contrast angiography and intraPlaque haemorrhage (SNAP) imaging: a magnetic resonance vessel wall imaging study. Eur Radiol 2018;28:1681-6.
115. Wang J, Bornert P, Zhao H, et al. Simultaneous noncontrast angiography and intraplaque hemorrhage

(SNAP) imaging for carotid atherosclerotic disease evaluation. Magn Reson Med 2013;69:337-45.
116. Fan ZY, Yu W, Xie YB, et al. Multi-contrast atherosclerosis characterization (MATCH) of carotid plaque with a single 5-min scan: technical development and clinical feasibility. J Cardiovasc Magn Reson 2014;16:53-64.
117. Dai Y, Lv P, Lin J, et al. Comparison study between multicontrast atherosclerosis characterization (MATCH) and conventional multicontrast MRI of carotid plaque with histology validation. J Magn Reson Imaging 2017;45:764-70.
118. Bucerius J, Hyafil F, Verberne HJ, et al. Position paper of the Cardiovascular Committee of the European Association of Nuclear Medicine (EANM) on PET imaging of atherosclerosis. Eur J Nucl Med Mol Imaging 2016;43:780-92.
119. Evans NR, Tarkin JM, Chowdhury MM, et al. PET Imaging of Atherosclerotic Disease: Advancing Plaque Assessment from Anatomy to Pathophysiology. Curr Atheroscler Rep 2016;18:30.
120. Moghbel M, Al-Zaghal A, Werner TJ, et al. The Role of PET in Evaluating Atherosclerosis: A Critical Review. Semin Nucl Med 2018;48:488-97.
121. Kwee RM, Truijman MT, Mess WH, et al. Potential of integrated [18F] fluorodeoxyglucose positron-emission tomography/CT in identifying vulnerable carotid plaques. AJNR Am J Neuroradiol 2011;32:950-4.
122. McKenney-Drake ML, Moghbel MC, Paydary K, et al. (18)F-NaF and (18)F-FDG as molecular probes in the evaluation of atherosclerosis. Eur J Nucl Med Mol Imaging 2018;45:2190-200.
123. Rudd JH, Warburton EA, Fryer TD, et al. Imaging atherosclerotic plaque inflammation with [18F]-fluorodeoxyglucose positron emission tomography. Circulation 2002;105:2708-11.
124. Pedersen SF, Sandholt BV, Keller SH, et al. 64Cu-DOTATATE PET/MRI for Detection of Activated Macrophages in Carotid Atherosclerotic Plaques: Studies in Patients Undergoing Endarterectomy. Arterioscler Thromb Vasc Biol 2015;35:1696-703.
125. Lee R, Kim J, Paeng JC, et al. Measurement of (68) Ga-DOTATOC Uptake in the Thoracic Aorta and Its Correlation with Cardiovascular Risk. Nucl Med Mol Imaging 2018;52:279-86.
126. Vöö S, Kwee RM, Sluimer JC, et al. Imaging Intraplaque Inflammation in Carotid Atherosclerosis With 18F-Fluorocholine Positron Emission Tomography-Computed Tomography: Prospective Study on Vulnerable Atheroma With Immunohistochemical Validation. Circ Cardiovasc Imaging 2016. doi: 10.1161/CIRCIMAGING.115.004467.
127. Li X, Heber D, Leike T, et al. [68Ga]Pentixafor-PET/MRI for the detection of Chemokine receptor 4 expression in atherosclerotic plaques. Eur J Nucl Med Mol Imaging 2018;45:558-66.
128. Dweck MR, Jenkins WS, Vesey AT, et al. 18F-sodium fluoride uptake is a marker of active calcification and disease progression in patients with aortic stenosis. Circ Cardiovasc Imaging 2014;7:371-8.
129. Zhang Y, Li H, Jia Y, et al. Noninvasive Assessment of Carotid Plaques Calcification by (18)F-Sodium Fluoride Accumulation: Correlation with Pathology. J Stroke Cerebrovasc Dis 2018;27:1796-801.
130. van der Valk FM, Sluimer JC, Voo SA, et al. In Vivo Imaging of Hypoxia in Atherosclerotic Plaques in Humans. JACC Cardiovasc Imaging 2015;8:1340-1.
131. Fernandez-Friera L, Fuster V, Lopez-Melgar B, et al. Vascular Inflammation in Subclinical Atherosclerosis Detected by Hybrid PET/MRI. J Am Coll Cardiol 2019;73:1371-82.
132. Bachi K, Mani V, Kaufman AE, et al. Imaging plaque inflammation in asymptomatic cocaine addicted individuals with simultaneous positron emission tomography/magnetic resonance imaging. World J Radiol 2019;11:62-73.
133. Hyafil F, Schindler A, Sepp D, et al. High-risk plaque features can be detected in non-stenotic carotid plaques of patients with ischaemic stroke classified as cryptogenic using combined (18)F-FDG PET/MR imaging. Eur J Nucl Med Mol Imaging 2016;43:270-9.
134. Li X, Heber D, Rausch I, et al. Quantitative assessment of atherosclerotic plaques on (18)F-FDG PET/MRI: comparison with a PET/CT hybrid system. Eur J Nucl Med Mol Imaging 2016;43:1503-12.
135. Ripa RS, Knudsen A, Hag AM, et al. Feasibility of simultaneous PET/MR of the carotid artery: first clinical experience and comparison to PET/CT. Am J Nucl Med Mol Imaging 2013;3:361-71.
136. Andrews JPM, MacNaught G, Moss AJ, et al. Cardiovascular 18F-fluoride positron emission tomography-magnetic resonance imaging: A comparison study. J Nucl Cardiol 2019. [Epub ahead of print].
137. Munoz C, Kunze KP, Neji R, et al. Motion-corrected Whole-heart Simultaneous Cardiac MR/PET Imaging: Initial Clinical Experience. MAGNETOM Flash 2019:18-25.
138. Kato S, Kitagawa K, Ishida N, et al. Assessment of coronary artery disease using magnetic resonance coronary angiography: a national multicenter trial. J Am Coll

Cardiol 2010;56:983-91.
139. Sakuma H, Ichikawa Y, Chino S, et al. Detection of coronary artery stenosis with whole-heart coronary magnetic resonance angiography. J Am Coll Cardiol 2006;48:1946-50.
140. Kim WY, Danias PG, Stuber M, et al. Coronary magnetic resonance angiography for the detection of coronary stenoses. N Engl J Med 2001;345:1863-9.
141. Henningsson M, Shome J, Bratis K, et al. Diagnostic performance of image navigated coronary CMR angiography in patients with coronary artery disease. J Cardiovasc Magn Reson 2017;19:68.
142. Jansen CHP, Perera D, Wiethoff AJ, et al. Contrast-enhanced magnetic resonance imaging for the detection of ruptured coronary plaques in patients with acute myocardial infarction. PLoS One 2017;12:e0188292.
143. Fayad ZA, Fuster V, Fallon JT, et al. Noninvasive in vivo human coronary artery lumen and wall imaging using black-blood magnetic resonance imaging. Circulation 2000;102:506-10.
144. Noguchi T. High-intensity plaques as a novel surrogate marker of vulnerable coronary lesions? J Cardiol 2017;70:518-9.
145. Matsumoto K, Ehara S, Hasegawa T, et al. The signal intensity of coronary culprit lesions on T1-weighted magnetic resonance imaging is directly correlated with the accumulation of vulnerable morphologies. Int J Cardiol 2017;231:284-6.
146. Pozo E, Agudo-Quilez P, Rojas-Gonzalez A, et al. Noninvasive diagnosis of vulnerable coronary plaque. World J Cardiol 2016;8:520-33.
147. Kanaya T, Noguchi T, Otsuka F, et al. Optical coherence tomography-verified morphological correlates of high-intensity coronary plaques on non-contrast T1-weighted magnetic resonance imaging in patients with stable coronary artery disease. Eur Heart J Cardiovasc Imaging 2019;20:75-83.
148. Noguchi T, Kawasaki T, Tanaka A, et al. High-Intensity Signals in Coronary Plaques on Noncontrast T1-Weighted Magnetic Resonance Imaging as a Novel Determinant of Coronary Events. J Am Coll Cardiol 2014;63:989-99.
149. Saeed M, Van TA, Krug R, et al. Cardiac MR imaging: current status and future direction. Cardiovasc Diagn Ther 2015;5:290-310.
150. Xie Y, Kim YJ, Pang J, et al. Coronary Atherosclerosis T1-Weighed Characterization With Integrated Anatomical Reference: Comparison With High-Risk Plaque Features Detected by Invasive Coronary Imaging. JACC Cardiovasc Imaging 2017;10:637-48.
151. Ginami G, Neji R, Phinikaridou A, et al. Simultaneous bright- and black-blood whole-heart MRI for noncontrast enhanced coronary lumen and thrombus visualization. Magn Reson Med 2018;79:1460-72.
152. Dweck MR, Chow MW, Joshi NV, et al. Coronary arterial 18F-sodium fluoride uptake: a novel marker of plaque biology. J Am Coll Cardiol 2012;59:1539-48.
153. Joshi NV, Vesey AT, Williams MC, et al. 18F-fluoride positron emission tomography for identification of ruptured and high-risk coronary atherosclerotic plaques: a prospective clinical trial. Lancet 2014;383:705-13.
154. Iwatsuka R, Matsue Y, Yonetsu T, et al. Arterial inflammation measured by 18F-FDG-PET-CT to predict coronary events in older subjects. Atherosclerosis 2018;268:49-54.
155. Wykrzykowska J, Lehman S, Williams G, et al. Imaging of inflamed and vulnerable plaque in coronary arteries with 18F-FDG PET/CT in patients with suppression of myocardial uptake using a low-carbohydrate, high-fat preparation. J Nucl Med 2009;50:563-8.
156. Lohmann P, Kocher M, Ceccon G, et al. Combined FET PET/MRI radiomics differentiates radiation injury from recurrent brain metastasis. Neuroimage Clin 2018;20:537-42.
157. Lucia F, Visvikis D, Vallieres M, et al. External validation of a combined PET and MRI radiomics model for prediction of recurrence in cervical cancer patients treated with chemoradiotherapy. Eur J Nucl Med Mol Imaging 2019;46:864-77.
158. Antunes J, Viswanath S, Rusu M, et al. Radiomics Analysis on FLT-PET/MRI for Characterization of Early Treatment Response in Renal Cell Carcinoma: A Proof-of-Concept Study. Transl Oncol 2016;9:155-62.
159. Zaharchuk G. Next generation research applications for hybrid PET/MR and PET/CT imaging using deep learning. Eur J Nucl Med Mol Imaging 2019;46:2700-7.
160. Chen H, Zhang Y, Kalra MK, et al. Low-Dose CT With a Residual Encoder-Decoder Convolutional Neural Network. IEEE Trans Med Imaging 2017;36:2524-35.
161. Hammernik K, Klatzer T, Kobler E, et al. Learning a variational network for reconstruction of accelerated MRI data. Magn Reson Med 2018;79:3055-71.
162. van Engelen A, Niessen WJ, Klein S, et al. Atherosclerotic plaque component segmentation in combined carotid MRI and CTA data incorporating class label uncertainty. PLoS One 2014;9:e94840.
163. Ouyang J, Chen KT, Gong E, et al. Ultra-low-dose PET reconstruction using generative adversarial network with

feature matching and task-specific perceptual loss. Med Phys 2019;46:3555-64.
164. Xiang L, Qiao Y, Nie D, et al. Deep Auto-context Convolutional Neural Networks for Standard-Dose PET Image Estimation from Low-Dose PET/MRI. Neurocomputing 2017;267:406-16.
165. Xu J, Gong E, Pauly J, et al. 200x Low-dose PET Reconstruction using Deep Learning. arXiv preprint arXiv:171204119 2017.
166. Wei W, Poirion E, Bodini B, et al. Learning Myelin Content in Multiple Sclerosis from Multimodal MRI through Adversarial Training. MICCAI 2018 – 21st International Conference On Medical Image Computing & Computer Assisted Intervention. Granada, Spain: Springer, 2018.

Cite this article as: Aizaz M, Moonen RPM, van der Pol JAJ, Prieto C, Botnar RM, Kooi ME. PET/MRI of atherosclerosis. Cardiovasc Diagn Ther 2020;10(4):1120-1139. doi: 10.21037/cdt.2020.02.09

